Materials Today Bio 28 (2024) 101222

Contents lists available at ScienceDirect

Materials Today Bio

journal homepage: www.journals.elsevier.com/materials-today-bio

A biomimetic targeted nanosystem delivering synergistic inhibitors for glioblastoma immune microenvironment reprogramming and treatment

Yulei Mu [a,1], Zhen Zhang [a,1], Huiqun Zhou [a,b], Min Jin [a,b], Liang Ma [a], Bangheng Liu [a,b], Cheng Ma [a,b], Xu Hu [a], Yi Zhang [c,**], Dong-An Wang [a,b,d,*]

[a] Department of Biomedical Engineering, City University of Hong Kong, 83 Tat Chee Avenue, Kowloon, Hong Kong
[b] Karolinska Institutet Ming Wai Lau Centre for Reparative Medicine, HKSTP, Sha Tin, Hong Kong
[c] School of Integrated Circuit Science and Engineering, University of Electronic Science and Engineering of China, Chengdu, Sichuan, China
[d] Shenzhen Research Institute, City University of Hong Kong, Shenzhen, China

ARTICLE INFO

Keywords:
Glioblastoma
Small-molecule inhibitors
CXCL12/CXCR4 axis
mTOR pathways
Blood-brain barrier

ABSTRACT

Efficient drug delivery across the blood-brain barrier is imperative for treating glioblastoma (GBM). This study utilized the GBM cell membrane to construct a biomimetic targeted nanosystem (GMNPs@AMD/RAPA) that hierarchically releases the CXCR4 antagonist AMD3100 and the mTOR pathway inhibitor rapamycin (RAPA) for reprogramming the tumor immune microenvironment and suppressing the progression of GBM. By initially inhibiting the CXCL12/CXCR4 axis, the tumor microenvironment (TME) was reprogrammed to enhance the infiltration of cytotoxic T lymphocytes (CTLs) into the TME while suppressing tumor cell survival, proliferation, and angiogenesis. Subsequently, through further cellular uptake and degradation of the nanoparticles, the mTOR pathway inhibitor RAPA was released, further suppressing the tumor progression. This study successfully combined chemotherapy and immunotherapy, achieving effective synergistic therapeutic effects, and suppressing the progression of GBM.

1. Introduction

Glioblastoma (GBM) is one of the most prevalent types of malignant brain tumor, characterized by its high invasiveness, accounting for around 49 % of all malignant brain tumors [1]. Treatments of GBM encounter substantial challenges arising from the distinctive characteristics of the tumor microenvironment (TME), encompassing the existence of the blood-brain barrier (BBB) and the immunosuppressive nature of GBM [2,3]. Additionally, conventional treatments for GBM, such as chemotherapy and radiation therapy, are likely to exacerbate immunosuppression, potentially fostering tumor recurrence [4,5]. Even though the short-term survival rate has seen slight improvement, the overall prognosis for GBM remains poor, with a median survival of less than 2 years and a high recurrence rate [6]. Therefore, the development of innovative targeted therapeutic strategies capable of modulating immune responses within the TME is crucial for the effective treatment of GBM.

In recent years, targeting the CXCL12/CXCR4 axis for the reprogramming of the tumor immune microenvironment has emerged as a highly promising approach in tumor therapeutics [7–10]. The surface expression of CXCR4 is evident across a range of cell types, encompassing stem cells, immune cells, and cancer cells. The CXCL12/CXCR4 axis exerts a crucial influence on multiple physiological processes, including hematopoiesis, embryonic development, immune response, and cancer metastasis [11–13]. The accumulation of antigen-specific $CD8^+$ T cells within tumors is a prerequisite for effective immune therapy. Inhibiting CXCR4 restricts the egress of T cells from TME, thereby enhancing their retention within the TME, augmenting T cell quality, and improving the efficacy of immunotherapy [14].

Meanwhile, CXCR4 is widely expressed in cancer cells, promoting tumor progression, angiogenesis, metastasis, and survival [15], and CXCR4 antagonists exhibit anti-tumor activity across various malignancies [2,16–20]. In GBM, the CXCL12/CXCR4 axis enhances tumor growth by facilitating tumor cell proliferation and stimulating tumor

* Corresponding author. Department of Biomedical Engineering City University of Hong Kong 83 Tat Chee Avenue, Kowloon, Hong Kong.
** Corresponding author. School of Integrated Circuit Science and Engineering, University of Electronic Science and Engineering of China, Chengdu, Sichuan, China.
E-mail addresses: yi_zhang@uestc.edu.cn (Y. Zhang), dwang229@cityu.edu.hk (D.-A. Wang).
[1] Equal Contribution.

https://doi.org/10.1016/j.mtbio.2024.101222
Received 3 June 2024; Received in revised form 29 August 2024; Accepted 31 August 2024
Available online 1 September 2024

angiogenesis through vascular endothelial growth factor (VEGF) released by GBM stem cells [21]. Therefore, by inhibiting the CXCL12/CXCR4 axis, it is possible to preemptively suppress tumor progression and influence TME and tumor angiogenesis.

The mammalian target of the rapamycin (mTOR) pathway plays a crucial role in regulating gene transcription and protein synthesis, thereby controlling cell proliferation and immune cell differentiation[21]. The PI3K/mTOR pathway, which is frequently hyperactivated in tumors, has been implicated in promoting GBM cell viability, tumor formation, and modulation of tumor metabolism [22]. Consequently, it has emerged as a prominent focus in anti-cancer therapeutic research [23,24]. However, excessive utilization of PI3K/mTOR pathway inhibitors during treatment leads to elevated CXCL12/CXCR4 axis levels, resulting in acquired resistance and immune suppression [25]. Therefore, simultaneous inhibition of CXCR4 and mTOR provides a promising therapeutic approach for GBM by modulating the crosstalk between the PI3K/mTOR pathway and the CXCL12/CXCR4 axis.

Despite the potential of CXCR4 antagonist AMD3100 [26] and mTOR inhibitor rapamycin (RAPA) in GBM treatment, their widespread clinical application is limited by suboptimal pharmacokinetics, long-term toxicity resulting from non-specific targeting, and the existence of BBB [18,27,28]. Recent progress in medicine has unveiled an intriguing therapeutic platform −tumor cell membrane-coated nanoparticles [29,30] – as an effective drug delivery system. Tumor homologous proteins and cell adhesion-related proteins in cell membrane coatings facilitate specific interactions with tumor cells, promoting the adhesion and internalization of nanoparticles to target cells [31], thereby improving treatment efficacy, reducing the adverse impact on normal cells, and minimizing damage to the organisms [32]. U87-MG cell membrane-coated nanoparticles were utilized for targeted delivery to homologous tumor sites in mice models, facilitating the intracellular uptake of DOX (doxorubicin) within tumor cells was reported before [33]. In the event of immunotherapy, the cell membrane harbors numerous tumor-associated antigens (TAAs) capable of promoting anti-tumor immunity and enhancing the effectiveness of immunotherapy [29].

In this study, we constructed a nanosystem (GMNPs@AMD/RAPA) wherein AMD3100 and RAPA were self-assembled into cell membrane-coated poly (lactic-co-glycolic acid) (PLGA) nanoparticles, enabling the sequential inhibition of the CXCL12/CXCR4 axis and mTOR signaling pathway, as shown in Fig. 1. This nanosystem led to the following outcomes: (1) GMNPs@AMD/RAPA crossed the blood-brain barrier (BBB) and accumulated in the TME. Additionally, GBM cell membrane coatings presented TAAs, leading to immunostimulation. (2) AMD3100 specifically binding to the CXCR4 protein domains on the cell membrane surface with higher affinity, facilitates the rapid release of AMD3100 from GMNPs@AMD/RAPA, resulting in the simultaneous inhibition of tumor cell survival, proliferation, and invasion while increasing the retention of cytotoxic T lymphocytes (CTLs) in the TME and promoting the activation of dendritic cells (DCs). (3) Subsequent internalization of

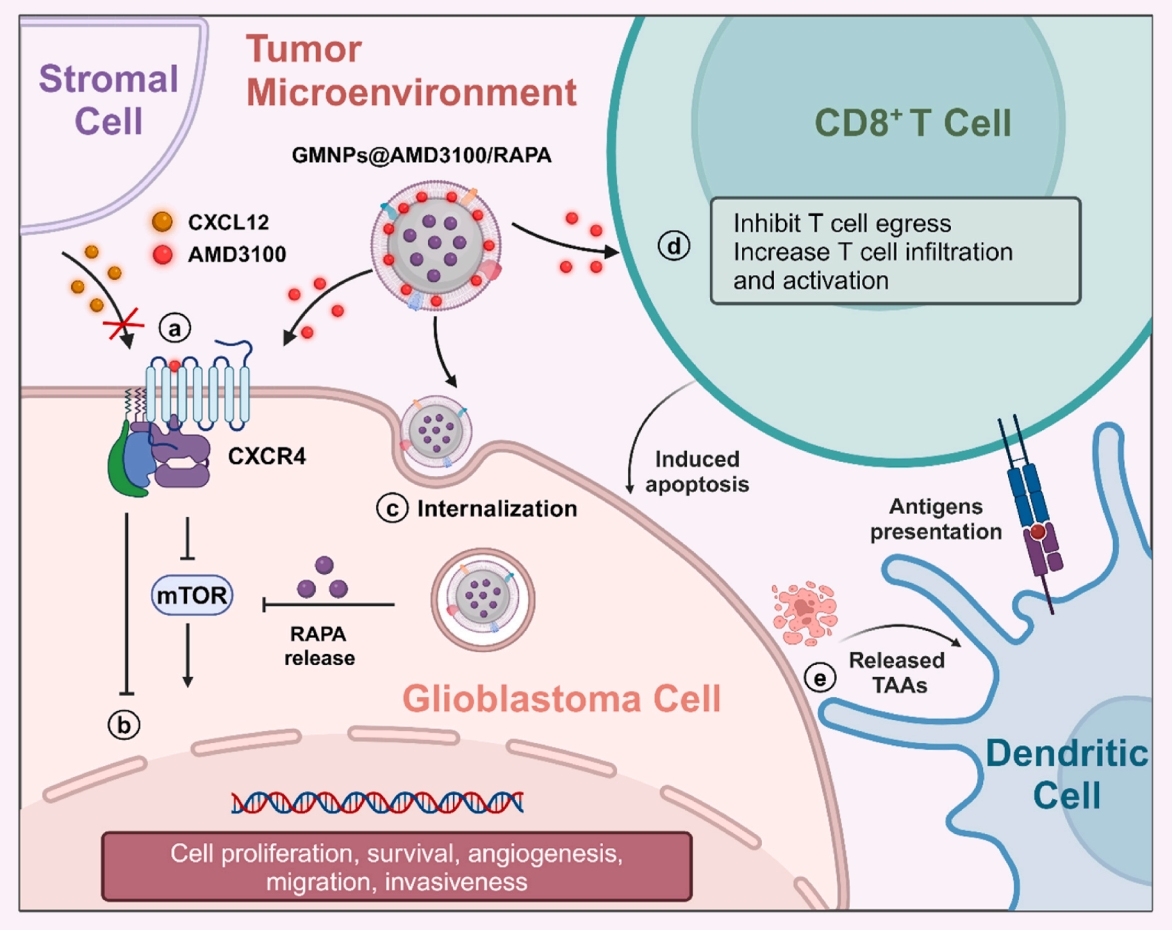

Fig. 1. Schematic of the therapeutic effect of GMNPs@AMD/RAPA in the TME. a GMNPs@AMD/RAPA, enriched in the tumor TME, first release AMD3100, which exhibits high affinity to the CXCR4 protein, selectively inhibiting the CXCL12/CXCR4 axis. **b** Downstream pathways of CXCR4 in tumor cells are inhibited resulting in the inhibition of tumor progression. **c** Further internalization of GMNPs@AMD/RAPA into tumor cells, followed by intracellular degradation and release of RAPA, leading to the inhibition of the mTOR pathway. **d** Release of AMD3100 in the TME inhibits the egress of $CD8^+$ T cells from the TME and increases their infiltration into the tumor. **e** TAAs released by tumor apoptosis increase the activation of dendritic cells. Created with BioRender.com.

GMNPs@AMD/RAPA by tumor cells facilitated intracellular degradation, resulting in the controlled release of RAPA within tumor cells, further suppressing the mTOR pathway and inhibiting tumor progression. This targeted and sequential delivery approach improved drug utilization, and inhibited crosstalk between the CXCL12/CXCR4 axis and mTOR pathway, thereby preventing mTOR drug resistance. It also modulated the tumor immune microenvironment, enhancing the infiltration and activation of $CD8^+$ T cells, further enhancing anti-tumor immune responses and inhibiting tumor progression.

2. Materials and methods

2.1. Synthesis and characterization of GMNPs@AMD/RAPA

To prepare NPs loaded with RAPA and AMD3100 (NPs@AMD/RAPA), 10 mg of 0.67 dL/g acid-terminated 50:50 poly (lactic-co-glycolic acid) (PLGA) and 1 mg of RAPA (Rapamycin, Meilunbio) were dissolved in 1 mL of acetone. The mixture was then sonicated to ensure thorough mixing. Subsequently, the mixture was added into 3 mL of 1 mg/mL plerixafor octahydrochloride (AMD3100, MedChemExpress) at 4 °C at a rate of 0.3 mL/min using a syringe pump (Aladdin). Acetone was then volatilized for 2 h while stirring at 800 rpm and then removed by rotary evaporation under reduced pressure at room temperature (RT). The resultant NPs@AMD/RAPA were collected through centrifugation at 4 °C. To prepare GBM cell membrane-coated NPs@AMD/RAPA (GMNPs@AMD/RAPA), U-87 MG cell membranes are extracted by the cell membrane and cytosol protein extraction kit (Beyotime). The membrane protein concentration was quantified by employing the BCA Protein Assay. Subsequently, extracted cell membranes and NPs@AMD/RAPA were mixed at a 1:1 wt ratio of polymer to membrane protein. The mixture was sonicated for 2 min and then extruded through a Mini-Extruder with a 200-nm polycarbonate membrane (Avanti Polar Lipids). Unless otherwise specified, chemical reagents were purchased from Sigma-Aldrich (USA).

Size and zeta potential were then detected by a dynamic light scattering spectrometer (DLS, Malvern Zeta Sizer ZEN3600). PDI (polydispersity index) of nanoparticles was analyzed by ZS Xplorer software. The morphology of the nanoparticles was characterized by an environmental scanning electron microscope (SEM, FEI Quanta 250) and transmission electron microscope (TEM, HT7700). Drug loading efficiency (LC) and encapsulation efficiency (EE) were evaluated employing a UV spectrophotometer (SpectraMax M3, MOLECULAR devices). Loading capacity (LC) = (mass of drug loaded in NPs)/[(mass of NPs)]. EE = (mass of drug loaded in NPs)/(mass of drug in formulation). Drug release of RAPA and AMD3100 was detected separately by UV spectrophotometer at the wavelength of 277 nm and 215 nm. GMNPs@AMD/RAPA (5 mg/mL, 1 mL) were added to a disposable dialysis membrane (MWCO: 2000 Da) with 15 mL PBST as the release medium. At different time points, 1.5 mL of the release medium was replaced for analysis.

SDS-PAGE, Western blotting, and proteomic analysis were employed to evaluate the inherent biological functional proteins within the cell membrane coating of GMNPs. The Western blotting analysis utilized *anti*-integrin alpha 5 antibody (Abcam, ab112183), *anti*-integrin beta 1 antibody (Abcam, ab183666), *anti*-integrin alpha 3 antibody (Proteintech, 66070-lg), CD44 antibody (Proteintech, 60224-1-Ig), goat anti-rabbit IgG H&L (HRP) (Abcam, ab205718), goat anti-mouse IgG H&L (HRP) (Abcam, ab205719), *anti*-integrin alpha 5 antibody (Abcam, ab112183).

2.2. Cell culture

U-87 MG cells were cultured in Minimum Essential Medium (MEM) supplemented with Non-Essential Amino Acids, 10 % fetal bovine serum (FBS), and 1 % penicillin-streptomycin at 37 °C in 5 % CO_2. U-87 MG cells (Procell, China), U-87 MG-Luc cells (IMMOCELL, China), G422 cells (IMMOCELL, China), G422-Luc cells (IMMOCELL, China), bEnd.3 cells (Procell, China), and RAW264.7 cells (ATCC, USA), were cultured in Dulbecco's Modified Eagle's Medium (DMEM) supplemented with 10 % FBS, and 1 % PS. Reagents used for cell culture were purchased from Thermo Fisher Scientific (USA).

2.3. Cellular uptake

The bEnd.3 cells were incubated with 0.1 mg/mL NPs and GMNPs, respectively. Flow cytometry was employed to quantify the intracellular. The data collected from the flow cytometer (BD FACSVerse™) were processed using FlowJo software to calculate the mean fluorescence intensity (MFI).

2.4. In vitro blood-brain barrier model construction

To construct the *in vitro* blood-brain barrier (BBB) model, 5×10^4 bEnd.3 cells were seeded on 12-well Transwell inserts with 3.0 μm polycarbonate membrane precoated with Matrigel (BD, 356234). 10^5 U-87 MG cells per well were concurrently seeded in the lower chambers. The transendothelial electrical resistance (TEER) values were measured using a volt-ohmmeter (Millicell ERS-2, Merck), and wells with TEER values exceeding 150 Ω cm^2 were selected for subsequent experiments. bEnd.3 and U-87 MG cell membranes were stained with DiD (1,1′-Dioctadecyl-3,3,3′,3′-Tetramethylindodicarbocyanine, Invitrogen). A total of 100 μL of 1 mg/mL DiO (3,3′-Dioctadecyloxacarbocyanine Perchlorate, Invitrogen) loaded NPs and GMNPs were separately introduced into the upper chambers of the Transwell system. After incubation for 4 h, the cellular uptake was characterized by CLSM. Flow cytometry was employed to assess U-87 MG cellular uptake quantitatively.

2.5. Construction of the orthotopic GBM model and evaluation of bioluminescence signals for brain tumor progression

The orthotopic intracranial GBM model was established through stereotaxic injection of U-87 MG-Luc cells or G422-Luc cells into male nude mice or C57BL/6 mice aged 6–8 weeks. 4×10^5 GBM cells were injected into the mice's brains (Medio-Lateral = −1.5 mm, Antero-Posterior = 1.5 mm, Dorso-Ventral = −3.5 mm, relative to bregma) using a sterile 5 μL Hamilton syringe attached to the Rotational Digital Stereotaxic Frame (RWD Life Science). Following the injection, the incisions on the mice's scalps were sutured, and their recovery was monitored. For the assessment of brain tumor development, the mice were intraperitoneally injected with 15 mg/mL of D-Luciferin potassium salt solution (Beyotime), with a dosage of 10 μL per gram of body weight. Tumors were visualized 15–20 min later using the In Vivo Imaging System Spectrum (IVIS, Perkin Elmer) to detect the bioluminescence signal.

2.6. In vivo biodistribution analysis and therapeutic intervention in GBM

125 μL of DiR (1,1′-Dioctadecyl-3,3,3′,3′-Tetramethylindotricarbocyanine Iodide, Invitrogen)-labeled nanoparticles suspended in PBS were administered to the mice via a mice tail vein injection device. The distribution of fluorescent signals in the mice was observed and analyzed using the IVIS. After the intravenous injection, the mice were euthanized, and the organs were subjected to IVIS imaging. Fluorescent intensity within regions of interest (ROIs) was quantified using the PerkinElmer IVIS Spectrum software. 125 μL of 1 mg/mL nanoparticles were administered to tumor-bearing C57BL/6 mice via tail vein injections at 48-h intervals, and the progression of the tumor was assessed by detecting bioluminescent signals using the IVIS system.

2.7. Hematoxylin and eosin (H&E) staining of animal tissues

5 μm-thick paraffin sections of the harvested organs were obtained

using a rotary microtome (Leica RM2265) for H&E staining. For cryosectioning, the tissues were sectioned into 10 μm-thick slices using a cryostat (CryoStar NX70). Following staining, the tissue sections underwent a dehydration process, were mounted with coverslips, and imaged using a microscope (Nikon Eclipse Ti2-E).

2.8. Effects of GMNPs@AMD/RAPA on cell invasion

The impact of nanoparticles on the invasive behavior of GBM cells towards brain microvascular endothelial cells (BMECs) was investigated utilizing 8.0-μm Transwell inserts. 1×10^4 U-87 MG cells were seeded onto the 8.0-μm polycarbonate membranes 24-well Transwell insert precoated with Matrigel (BD, 356234). 2×10^4 bEnd.3 cells per well were seeded in the lower chamber. The upper chamber was filled with 200 μl serum-free culture medium 0.1 mg/mL nanoparticle solution, while the lower chamber contained 500 μl culture medium supplemented with 10 % serum. After 24 h of incubation, the cells on the apical surface of the inserts were gently eliminated. The remaining cells on the basal surface of the inserts were stained with a crystal violet staining solution (Beyotime). Observation of the stained cells was performed using a microscope, and the extent of cell invasion was quantitatively assessed using ImageJ.

2.9. Cellular endocytosis mechanism of GMNPs

BEnd.3 cells were incubated with GMNPs for 2 h to investigate the endocytic pathways. Before incubation, the cells were stained with the membrane dye DiD and pre-treated with 5.7 μM hydroxy-dynasore (MCE), 5 μM blebbistatin (MCE), 10 μM chlorpromazine (MCE), or 10 μM cytochalasin D (Aladdin) for 60 min at 37 °C followed by characterization with CLSM. The Colocalization Finder plugin of the ImageJ software was used to calculate the colocalization coefficients.

2.10. In vitro lysosomal escape of GMNPs

RAW 264.7 or U-87 MG cells in confocal dishes were incubated with Lyso-Tracker red. Nuclei were stained with Hoechst 33342 solution. NPs and GMNPs were then incubated with the stained cells and observed with CLSM to study the colocalization of lysosomes and nanoparticles.

2.11. Flow cytometry analysis of mice brain tissue

C57BL/6 mice were euthanized for brain tissue collection. The brain tissue was minced using scissors and processed into a single-cell suspension. The suspension was then incubated with anti-mice APC anti-mice CD3 (Biolegend, 100236), FITC anti-mice CD8b.2 (Biolegend, 140404), and PE anti-mouse CD4 (Biolegend, 100408) Antibody antibodies for T cell staining, or with PE anti-mice CD11c (Biolegend, 117308) and APC anti-mice CD86 (Biolegend, 105012) antibodies for dendritic cell staining. Use a flow cytometer (BD FACSVerse™) to characterize stained cells and FlowJo software to analyze data.

2.12. Immunohistochemical staining of vascular in mice brain tissue

5 μm-thick mice brain paraffin sections were prepared for Immunohistochemical (IHC) staining. The sections were incubated with the primary antibody against Vascular Endothelial Growth Factor Receptor 2 (VEGFR2) (Abcam, ab2349) after antigen retrieval and blocking. Subsequently, the sections were treated with 3 % H_2O_2 and incubated with the secondary antibody (Proteintech, PK10006). DAB staining was performed for VEGFR2, and hematoxylin staining was used for nuclear staining.

2.13. Animal care

All animals used in this study were provided by the Laboratory Animal Research Unit (LARU) and were conducted following the regulations of the Department of Health. All animal experiments received the approval from Animal Research Ethics Sub-Committee (AEC, #A-0828). When mice displayed advanced tumor burden symptoms, such as weight loss exceeding 20 %, a hunched posture, prominent cranial bones, and pronounced neurological symptoms, euthanasia was conducted to minimize suffering and ensure compliance with ethical considerations.

2.14. Statistical analysis

Data were subjected to statistical analysis using GraphPad Prism 9.5.0. Statistical tests such as Student's t-test, one-way ANOVA, and two-way ANOVA were employed where appropriate. The results are presented as mean ± standard deviation (SD). *$p < 0.05$; **$p < 0.01$; ***$p < 0.001$; ****$p < 0.0001$; ns, not significant.

3. Results

3.1. Synthesis and characterization of the GMNPs@AMD/RAPA nanosystem

The synthesis of the GMNPs@AMD/RAPA nanosystem is illustrated in Fig. 2a. First, the GBM cell membrane-camouflaged nanoparticles (GMNPs) were synthesized as the nanocarrier. As shown in Fig. 2b and c, DLS measurements revealed that the particle sizes of the PLGA cores (NPs) and GMNPs were 140.1 ± 1.940 nm (PDI = 0.09951) and 151 ± 1.718 nm (PDI = 0.1078), respectively and the surface zeta potentials were −49.4 ± 6.180 mV and −35.43 ± 2.984 mV, respectively. The zeta potential of NPs loaded with AMD3100 (NPs@AMD) is 14.96 ± 1.025 mV, indicating successful electrostatic adsorption of positively charged AMD3100 onto the NPs. With the positive charged AMD3100 in formulation, the size of the nanoparticles had slightly condensed to 123.6 ± 2.487 nm (PDI = 0.05349). The size and the zeta potential of GMNPs@AMD/RAPA were measured at 153.4 ± 1.076 nm (PDI = 0.2609) and −14.7 ± 1.386 mV, indicating a decrease in negative charge due to the loading of AMD3100. The results obtained from SEM (Fig. S2) and TEM (Fig. 2e) analysis indicated that GMNPs possessed relatively uniform particle size and exhibited a core (PLGA) - shell (GBM cell membrane) structure. This observation confirmed the successful construction of GMNPs. Fig. 2d demonstrates that GMNPs maintain a constant size in 4 °C PBS for 6 weeks, indicating their long-term storage stability of the cell membrane coating. Moreover, fluorescence colocalization imaging of the NPs core and GBM cell membrane coating (GCM) of GMNPs after washing with PBS and 50 % FBS-PBS solution, revealed the stability of the cell membrane coating in serum (Fig. 2f).

To elucidate the protein composition associated with the cell membrane coating, we conducted proteomic analysis on GMNPs. Sodium dodecyl sulfate-polyacrylamide gel electrophoresis (SDS-PAGE) analysis was employed to reveal the absence of significant protein degradation after the coating process (Fig. 2j). Gene Ontology (GO) analysis of the GMNPs revealed a significant enrichment of cell adhesion related membrane proteins thereby conferring biomimetic attributes to the nanoparticles (Fig. 2g). The tumor cell adhesion-related membrane proteins identified by the proteomic analysis were quantified using the Intensity-Based Absolute Quantification (IBAQ) method (Fig. S3). GMNPs contained a substantial amount of tumor homologous adhesion-related proteins, such as integrins and cadherins, which increased the homologous targeting ability of GMNPs [34]. Western blotting analysis confirmed representative proteins including integrin β1, integrin α3, integrin α3, and CD44.

To ascertain the drug-loading capacity, the UV spectrum of AMD3100 and RAPA was measured (Fig. S4). The measurements and calculation showed that LC_{RAPA} was 3.49 % and EE_{RAPA} was 39.88 %. $LC_{AMD3100}$ = 9.01 %. $EE_{AMD3100}$ = 34.28 %. The results presented in Fig. 2h and i demonstrated the cumulative release profiles of AMD3100 and RAPA at 37 °C in PBS at pH 7.4 and pH 5.5. It was observed that

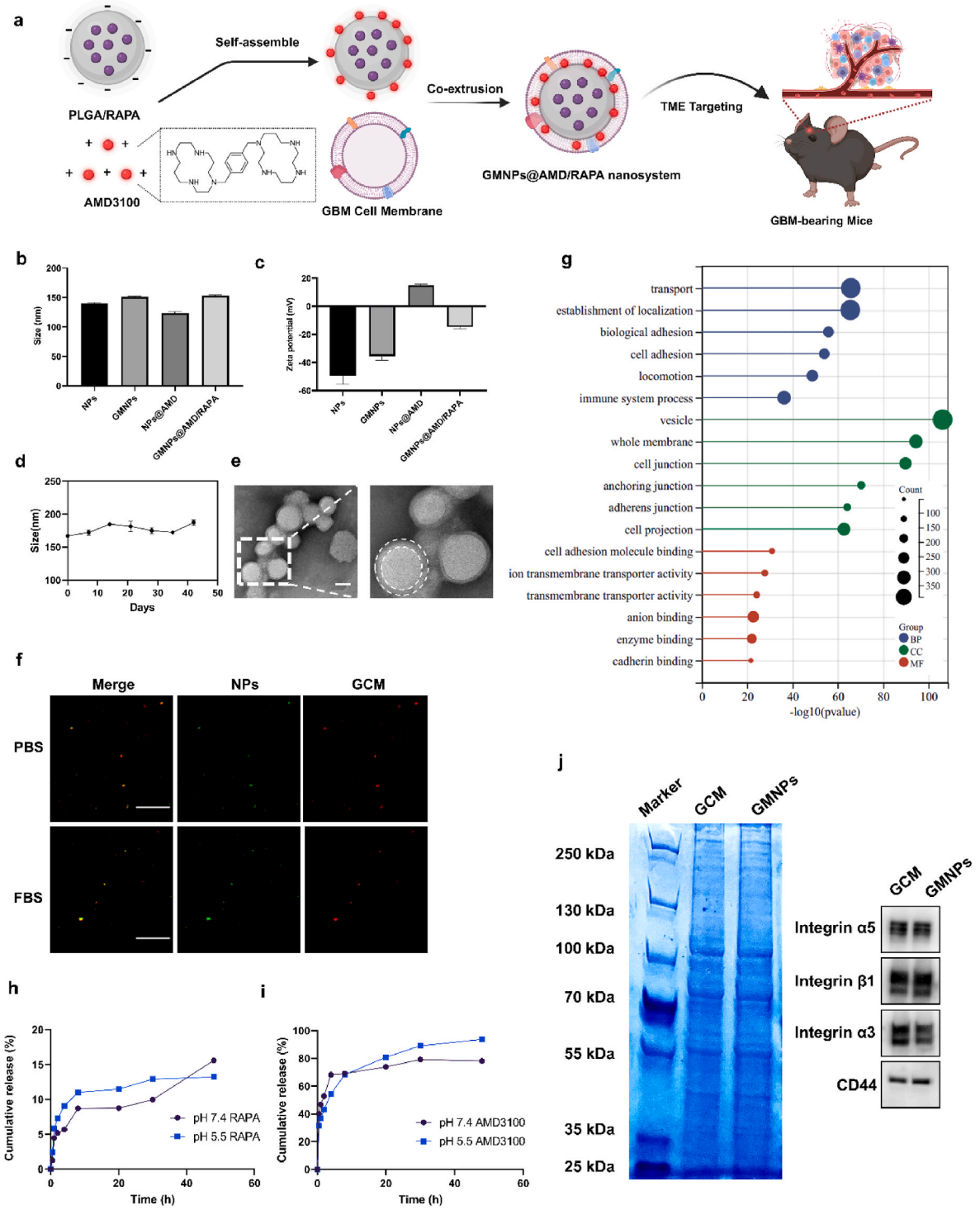

Fig. 2. Synthesis and characterization of the GMNPs@AMD/RAPA. a Schematic illustration of the construction of GMNPs@AMD/RAPA. b-c Particle hydrodynamic size (**b**) and surface zeta potential (**c**) of NPs, GMNPs, NPs@AMD, and GMNPs@AMD/RAPA measured by DLS. **d** Long-term size stability of GMNPs in PBS measured by DLS. **e** TEM analysis of the core-shell structure of GMNPs. Scale bars = 100 nm. **f** CLSM image of GMNPs washed by PBS and 50 % FBS. Scale bars = 50 μm **g** Proteomics Gene Ontology (GO) analysis of GMNPs. BP (biological process), CC (cellular component), MF (molecular function). **h-i** Cumulative RAPA (h) and AMD3100 (i) release of GMNPs@AMD/RAPA at pH 7.4 and pH 5.5 for 48 h **j** SDS-PAGE and Western Blot of GBM cell membrane coating and GMNPs.

AMD3100 exhibited rapid initial release within the first 2 h, with a release percentage of 52.89 % at pH 7.4 and 43.18 % at pH 5.5. In contrast, RAPA displayed a controlled release pattern over 48 h, with a release percentage of 15.59 % at pH 7.4 and 13.23 % at pH 5.5.

3.2. BBB penetration and tumor targeting of GMNPs@AMD/RAPA In vitro and In vivo

To evaluate the improvement effect of biomimetic cell membrane coating on the uptake capacity of NPs by BMECs, the cellular uptake of GMNPs by bEnd.3 cells were measured at 1, 2, 4, and 6 h. As shown in

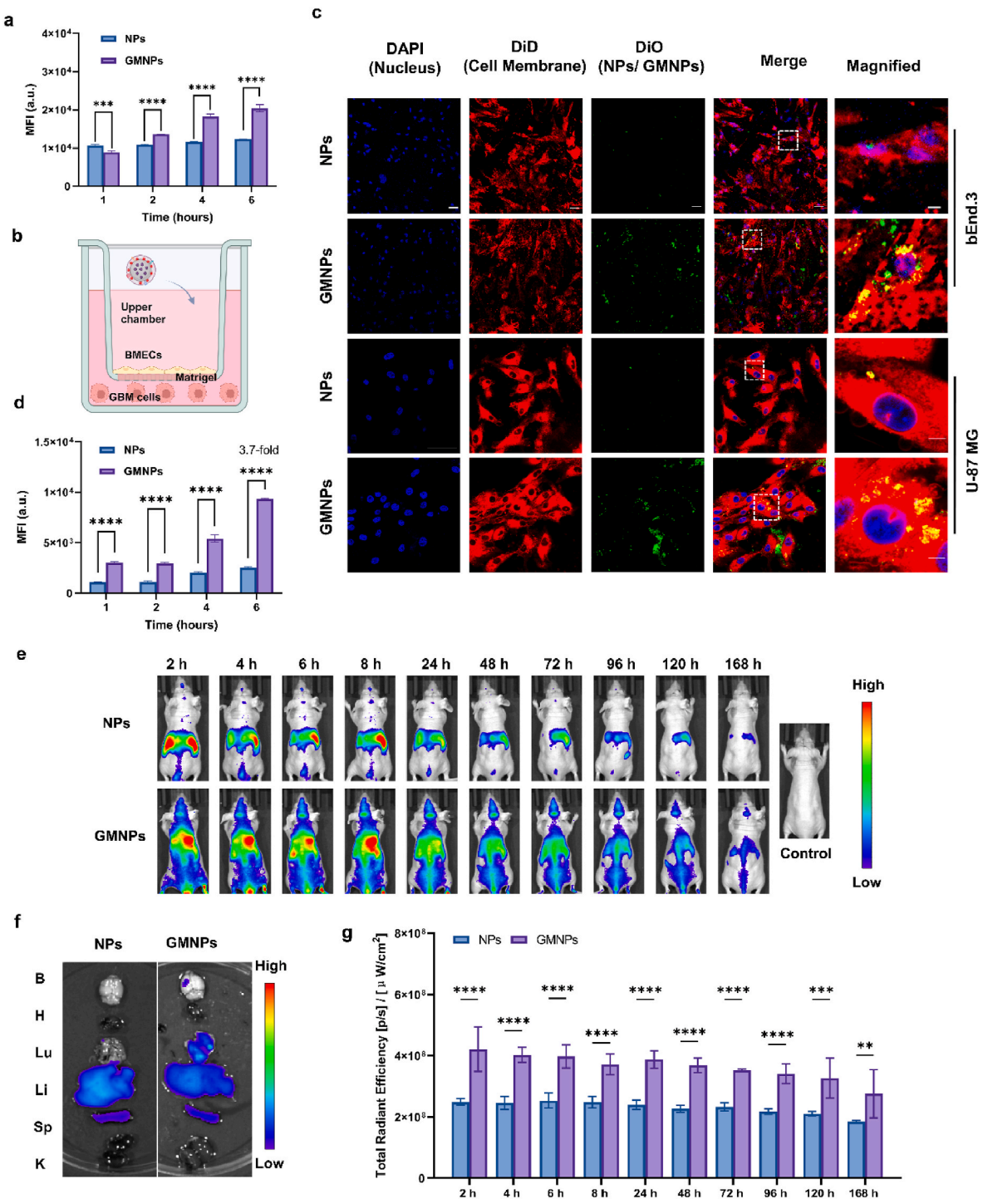

Fig. 3. Tumor targeting of GMNPs@AMD/RAPA *in vitro* and *in vivo*.

Fig. 3a, As illustrated in Fig. 3a, the uptake of GMNPs by bEnd.3 cells displayed a progressive escalation from 1h to 6h, whereas the uptake of NPs remained relatively constant. At the 6h, bEnd.3 cells exhibited a significantly higher cellular uptake of GMNPs compared to the NPs group, suggesting that the cell membrane coating effectively enhanced the internalization capacity within endothelial cells. Furthermore, to investigate the ability of GMNPs@AMD/RAPA to traverse the BBB, an *in vitro* model was established by employing bEnd.3 and U-87 MG GBM cells in a Transwell system, as illustrated in Fig. 3b. Upon achieving a transendothelial electrical resistance (TEER) value exceeding 150 Ω cm^2 on Day 9 (Fig. S5), NPs/DiO or GMNPs/DiO were introduced into the upper chamber. After a 4h incubation period, CLSM results revealed that GMNPs exhibited augmented penetration across BMECs and uptake by GBM cells compared to uncoated NPs (Fig. 3c). Nanoparticle uptake by U-87 MG cells in the lower chamber was assessed by flow cytometry (Fig. 3d), and the results indicated a substantial increase of GMNPs uptake by U-87 MG cells as time proceeded from 1 h, 2 h, 4 h–6 h, and the uptake was significantly higher than that of NPs. The results above underscore a significant improvement in the *in vitro* targeting ability of nanoparticles through homologous cell membrane coatings. Fluorescence colocalization of GMNPs with U87 cells lysosomes after incubating for 4h indicated the internalization of GMNPs by tumor cell

lysosomes, as shown in Fig. S6.

To confirm the *in vivo* brain tumor-targeting capability of GMNPs, an orthotopic mice GBM model was induced through intracranial transplantation of U-87 MG-Luc cells into nude mice. Bioluminescence signals were detected by In Vivo Imaging Spectrum (IVIS), and mice with stable brain tumors on Day 10 were selected for subsequent experiments (Fig. S7). NPs and GMNPs loaded with DiR were administered systemically via intravenous injection in tumor-bearing mice, facilitating the real-time monitoring of the biodistribution of NPs and GMNPs over time based on fluorescent signals. IVIS imaging results in Fig. 3e and Fig. S8 illustrated the tumor-targeting capability of GMNPs in the mice brain, while uncoated NPs exhibited minimal signal in the mice brain, implying no specific targeting capability. GMNPs achieved a high degree of brain accumulation within 24 h, which were subsequently metabolized by 168 h (Fig. 3g). *In vivo* imaging of organs at 24 h (Fig. 3f) further confirmed the accumulation of GMNPs in the mice brain, indicating the capability of brain targeting.

The H&E staining results of mice organs, including the heart, liver, spleen, lung, and kidney, depicted in Fig. S9, indicated that the administration of GMNPs did not impose any evident structural damage nor pathological alterations in these organs. These findings suggested that the targeted carrier GMNPs did not elicit discernible organ toxicity or adverse effects in these vital organs.

a Flow cytometry analysis quantified the Internalization of NPs and GMNPs by bEnd.3 cells. (n = 3). **b** Schematic illustration of using Transwell to construct an *in vitro* BBB model. **c** Representative CLSM images of the cell internalization of NPs and GMNPs crossing the Transwell BBB model. Scale bar = 50 μm (main image), 10 μm (magnified image). **d** Internalization of NPs and GMNPs by U-87 MG cells in the lower chamber of the Transwell system was quantified through flow cytometry analysis. (n = 3). **e** DiR fluorescence signals detected by IVIS at 2, 4, 6, 8, 24, 48, 72, 96, 120, and 168 h were used to characterize the biodistribution of NPs and GMNPs *in vivo*. **f** IVIS images of the ex vivo brain, heart, lungs, liver, spleen, and kidneys after 24 h of nanoparticle injection. **g** IVIS brain region statistics analysis of DiR signal at 2, 4, 6, 8, 24, 48, 72, 96, 120, and 168 h (n = 4).

3.3. Cellular uptake and antitumor efficacy of GMNPs@AMD/RAPA in vitro

To investigate the internalization pathways of GMNPs in BMECs, various inhibitors, including dynasore (a dynamin inhibitor), chlorpromazine (a clathrin inhibitor), cytochalasin D (an actin inhibitor), and blebbistatin (a myosin inhibitor), were used to pre-treat bEnd.3 cells. CLSM was utilized to visualize the cellular uptake of GMNPs by BMECs, as shown in Fig. 4a. By calculating the fluorescence colocalization coefficient between GMNPs and the cell membrane, the impact of different internalization pathways on GMNPs uptake was evaluated and compared, as depicted in Fig. 4b. Compared to the control group, significant inhibition of GMNPs uptake was observed in the presence of the inhibitors. The internalization of GMNPs by endothelial cells was notably regulated by dynamin (7.2-fold) and actin (14.6-fold), proving that the internalization process predominantly occurs through fast endophilin-mediated endocytosis (FEME) [35].

Nanoparticle clearance in the biological system relies on hepatic macrophages, known as Kupffer cells, located within the liver sinusoids. However, upon coating with GBM cell membrane, the uptake of nanoparticles by the liver is significantly reduced compared to bare PLGA NPs without the cell membrane camouflage. Fig. S10 illustrates that GMNPs exhibit a lower hepatic clearance rate compared to uncoated NPs, indicating their potential for prolonged systemic circulation. Furthermore, Fig. 4h showcases the nanoparticle uptake by RAW264.7 macrophages *in vitro* using flow cytometry. It was evident that the macrophage uptake of uncoated NPs peaked at 4 h, whereas the uptake of GMNPs was 4.2-fold lower compared to that of uncoated NPs. CLSM images and colocalization analysis using Lyso-Tracker Red staining of RAW264.7 cells demonstrated a significantly reduced uptake of GMNPs by lysosomes compared to NPs loaded with DiO dye (Fig. 4g and h).

Given the targeting effects of GMNPs, the subsequent objective is to assess the therapeutic efficacy of GMNPs@AMD/RAPA for treating GBM. The cytotoxicity of GMNPs@AMD/RAPA towards tumor cells was evaluated using the CCK-8 assay. Tumor cells were treated with 0.1 mg/mL GMNPs@AMD/RAPA for 24 and 48 h, followed by the assessment of cell viability. To investigate the inhibitory effects of AMD3100 on the CXCL12/CXCR4 axis, each group was supplemented with 100 ng/mL CXCL12. The results in Fig. 4f demonstrated that GMNPs@AMD/RAPA exhibited significant cytotoxicity towards tumor cells, achieving a toxicity of 76.02 % at 24 h and 47.51 % at 48 h. Furthermore, compared to the GMNPs@AMD or GMNPs/RAPA groups with equivalent concentrations of drugs as the GMNPs@AMD/RAPA group, the GMNPs@AMD/RAPA group exhibited significantly lower cell viability at 48 h, demonstrating the synergistic effect of AMD3100 and RAPA in GBM treatment.

To investigate the impact of simultaneous inhibition of the CXCR4 and mTOR pathways on tumor invasion, a Transwell *in vitro* co-culture model mimicking the GBM TME was constructed (Fig. 4e), the inhibitory effects of GMNPs@AMD/RAPA on the invasion of GBM cells into the bEnd.3 cells in the lower chamber of the Transwell system were investigated. As shown in Fig. 4c, after 24 h of incubation, the cells that adhered to the apical surface of the Transwell insert were gently removed. Subsequently, crystal violet staining was conducted on the tumor cells situated on the basal surface of the Transwell inserts. Fig. 4d presented the statistical analysis of the cell invasion rate. The results revealed that non-drug-loaded NPs and GMNPs did not exert any significant inhibitory effect on tumor invasion. However, NPs/RAPA and GMNPs/RAPA loaded with RAPA inhibited tumor invasion. Notably, GMNPs@AMD and GMNPs@AMD/RAPA loaded with AMD3100 demonstrated the most prominent suppression of tumor invasion. This indicated that GMNPs@AMD/RAPA significantly inhibited the invasion of GBM cells by suppressing the CXCL12/CXCR4 axis.

a Influence of dynasore, chlorpromazine hydrochloride, cytochalasin D, and blebbistatin on cellular uptake of GMNPs (green, labeled by DiO) in bEnd.3 cells (red stands for cell membrane labeled by DiD) as detected by CLSM. Scale bar = 50 μm (main image), 10 μm (magnified image). The data are shown as mean ± SD (n = 3). **b** The Pearson fluorescence colocalization coefficient of GMNPs and the cell membrane in Fig. 4a was quantitatively analyzed using ImageJ. (n = 3). **c** Crystal violet staining represents the impact of NPs, GMNPs, NPs/RAPA, GMNPs/RAPA, GMNPs@AMD, GMNPs@AMD/RAPA on GBM cell invasion ability. Scale bar = 500 μm (main images), 100 μm (magnified images). **d** Percentage of migration of GBM cells towards BMECs after incubation with different nanoparticles for 24 h, normalized to the migration of the control group. (n = 3). **e** Schematic illustration depicting the Transwell assay employed to investigate the invasiveness of GBM cells towards BMECs. **f** GBM Cell viability measured by CCK-8 assay at 24 h and 48 h after treatment with each formulation. (n = 4). **g** Characterization of fluorescence colocalization of nanoparticles uptake by RAW264.7 lysosomes using CLSM. Scale bar = 50 μm **h** The Pearson fluorescence colocalization coefficient of lysosomes (lyso-tracker red) and NPs or GMNPs (DiO) in Fig. 4g was quantitatively analyzed using ImageJ. **i** Cellular uptake of NPs and GMNPs in RAW264.7 characterized by flow cytometry. (n = 3).

3.4. Orthotopic GBM progression inhibition and anti-angiogenic effects by GMNPs@AMD/RAPA

To assess the anti-tumor efficacy of GMNPs@AMD/RAPA, an orthotopic tumor model was established in C57BL/6 mice. The tumor-bearing mice received intravenous injections of 125 μL of the drug-loaded nanosystem every 48 h for a total of 6 doses (Fig. 5a). Subsequently, the bioluminescent signals of GBM were monitored using IVIS imaging (Fig. 5b). Compared to the PBS group, GMNPs/RAPA,

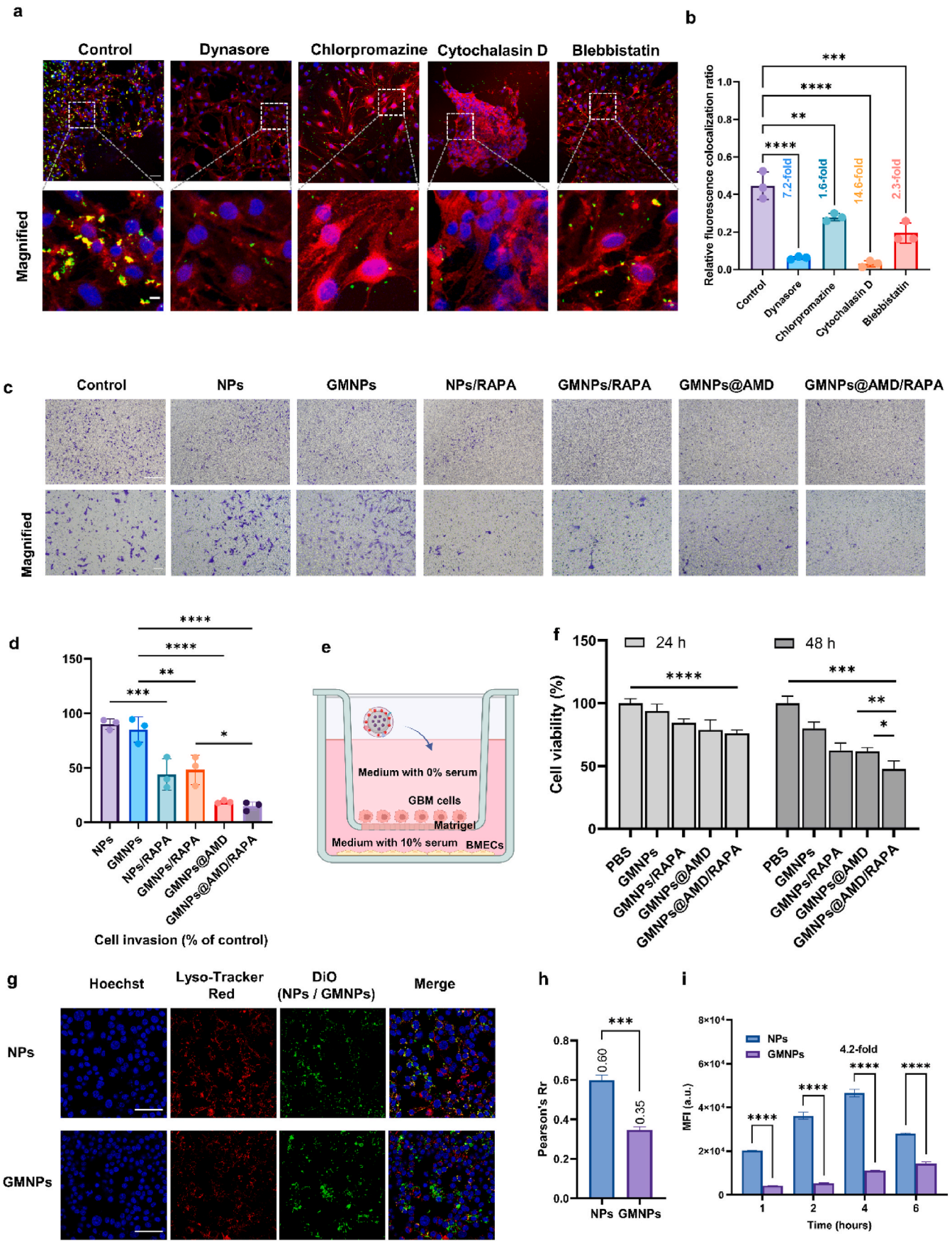

Fig. 4. *In vitro* cellular uptake and antitumor efficacy of GMNPs@AMD/RAPA

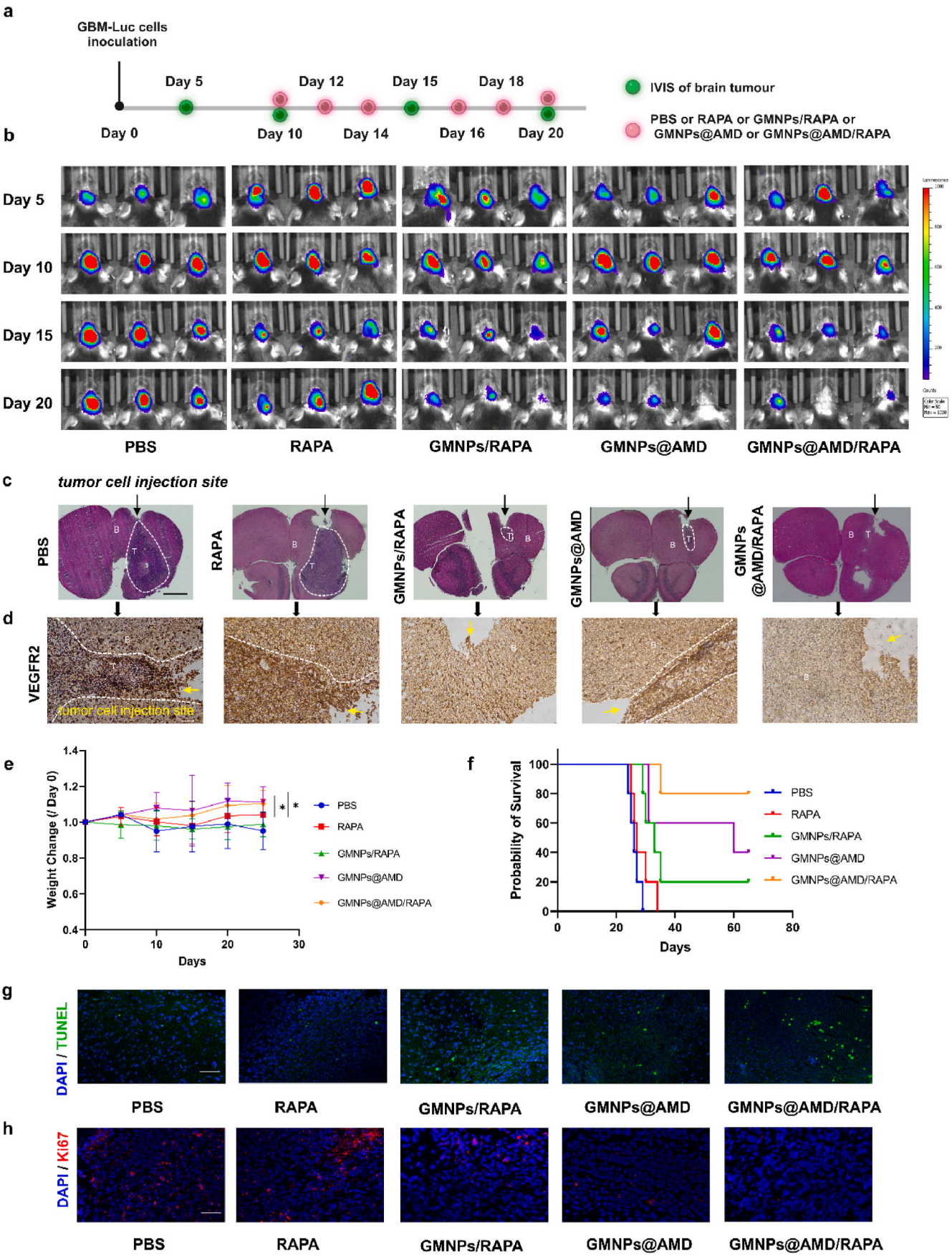

Fig. 5. The therapeutic efficacy of GMNPs@AMD/RAPA in orthotopic GBM treatment.

GMNPs@AMD, and GMNPs@AMD/RAPA groups exhibited a reduction in bioluminescent signals on day 20 after 6 doses. On day 20, the RAPA group showed an increase in bioluminescent signals. It can be observed that the progression of GBM was inhibited in groups treated with GMNPs/RAPA, GMNPs@AMD, and GMNPs@AMD/RAPA. Further confirmation of effective tumor suppression in mice treated with GMNPs@AMD/RAPA was obtained through histological staining of brain tissues with H&E (Fig. 5c).

IHC analysis was employed to assess the reduction of tumor angiogenesis. As depicted in Fig. 5d, IHC results of VEGFR2 in mice brain tissues following different treatments revealed a significant reduction in VEGFR2 expression in the GMNPs/RAPA, GMNPs@AMD, and GMNPs@AMD/RAPA groups, compared to the PBS and RAPA groups. Notably, the GMNPs/RAPA and GMNPs@AMD/RAPA groups exhibited a more pronounced decrease in VEGFR2 expression compared to the GMNPs@AMD group, indicating that the enhanced anti-angiogenesis effect was achieved through the targeted delivery of RAPA. Following treatment with GMNPs@AMD, GMNPs/RAPA, and GMNPs@AMD/RAPA, the TUNEL-positive signals in the tumor region of mice showed a significant increase (Fig. 5g), providing compelling evidence that the therapeutic intervention with GMNPs@AMD/RAPA effectively induces apoptosis in tumor cells. Ki67 staining indicated that GMNPs@AMD/RAPA inhibited the proliferation of GBM cells as shown in Fig. 5h.

Changes in body weight and survival rate were recorded throughout the treatment (Fig. 5e and f). The groups receiving treatment with GMNPs@AMD and GMNPs@AMD/RAPA exhibited significant weight gain compared to the PBS group on day 25. The improved survival rate of GBM-bearing mice in the GMNPs@AMD/RAPA treatment group demonstrated significant therapeutic efficacy.

a Schedule of tumor cell inoculation, GMNPs@AMD/RAPA administration, and IVIS imaging in C57BL/6 mice GBM model. **b** Bioluminescent IVIS images of intracranial G422-luc GBM-bearing mice after GMNPs@AMD/RAPA treatment. **c** H&E staining of representative paraffin-embedded brain sections at day 25 of different treating groups. The black arrows indicate the region of tumor cell injection. T represents the tumor area, and B represents normal brain tissue. Scale bar = 1000 μm **d** Representative image of IHC staining of VEGFR2 in different treatment groups on day 25. The yellow arrow indicates the tumor cell inoculation site. T represents the tumor area, and B represents normal brain tissue. Scale bars = 50 μm. **e** Relative body weight change after treatments. (n = 5). **f** Survival curve of mice after treatments. (n = 5). **g** Representative CLSM image of TUNEL staining of GBM tumor region in different treatment groups. Scale bar = 50 μm **h** Representative CLSM image of Ki67 staining of GBM tumor region in different treatment groups. Scale bar = 50 μm.

3.5. GMNPs@AMD/RAPA enhances immune cells activation

To evaluate the impact of GMNPs@AMD/RAPA in modulating the immune microenvironment, flow cytometry was utilized to characterize the activation of DCs and CTLs. Flow cytometry analysis of T cells in mice brain tissue suspensions post-treatment revealed a significant increase in the proportion of $CD3^+$ T cells within the TME in the GMNPs@AMD and GMNPs@AMD/RAPA groups after 6 doses of drugs (Fig. 6b). This observation indicates that GMNPs@AMD and GMNPs@AMD/RAPA effectively mitigate the immunosuppression induced by the RAPA. Consistently, as depicted in Fig. 6a and c, the proportion of $CD8^+$ T cells within the $CD3^+$ T cell population exhibited a similar trend, further corroborating the conclusion that the immune response was enhanced by GMNPs@AMD and GMNPs@AMD/RAPA. It was evident that AMD3100 significantly enhanced the infiltration of $CD8^+$ T cells into TME. The $CD4^+$ helper T cell to $CD8^+$ cytotoxic T cell ratio was assessed within the TME as depicted in Fig. 6d. It was observed that the GMNPs@AMD/RAPA group displayed a notable reduction in the $CD4^+/CD8^+$ ratio, suggesting an augmented abundance of cytotoxic T cells.

The activation status of DCs was investigated using flow cytometry, as depicted in Fig. 6e–g. The proportions of $CD11c^+CD86^+$ cells among all groups revealed a substantial elevation of activated DCs ($CD11c^+CD86^+$) in the GMNPs@AMD and GMNPs@AMD/RAPA groups compared to the PBS and RAPA groups, underscoring a higher level of activation of dendritic cells in the GMNPs@AMD and GMNPs@AMD/RAPA groups, an indication of enhanced immune response in these treatment groups.

a Flow cytometric quantification of $CD3^+CD8^+$ T cells in brain tissue of different treating groups after 6 doses at day 20. **b-d** Statistical analysis of the proportion of $CD3^+$ cells relative to the total number of single cells (**b**), $CD3^+CD8^+$ cells relative to $CD3^+$ cells (**c**), and $CD3^+CD4^+$ cells relative to $CD3^+CD8^+$ cells (**d**). **e** Flow cytometric quantification of $CD86^+CD11c^+$ cells of single cells in mice brain. **f** Histogram of $CD11c^+$ cells in brain tissue of different treating groups at day 20. **g** Statistical analysis of the proportion of $CD86^+$ cells of $CD11c^+$ cells quantified by flow cytometry. (n = 3).

3.6. Assessment of long-term organ histopathology and hematological safety

Long-term systemic administration of RAPA and AMD3100 poses risks of organ and hematological toxicity. Nevertheless, the encapsulation of AMD3100 and RAPA within GMNPs presents an effective approach to mitigating potential toxicity. In addition to the anti-tumor efficacy of GMNPs@AMD/RAPA, a comprehensive safety assessment was conducted in tumor-bearing C57BL/6 mice. The mice received 6 doses of drugs and underwent a 5-day recovery period. Histopathological examination of cryosections stained with H&E (Fig. 7a) and complete blood count (CBC) analysis (Fig. 7b–m) were performed to assess the potential toxicity of GMNPs@AMD/RAPA in the treated mice. H&E results indicated the absence of notable histopathological abnormalities in the examined organ samples. Furthermore, no statistically significant differences in the major blood parameters of the GBM-bearing mice peripheral blood were observed. These results indicated that GMNPs@AMD/RAPA did not induce any significant damage to major organs nor exhibited any hematological toxicity. Notably, following GMNPs@AMD treatment, a modest decrease of white blood cells [$(4.0 \pm 0.2532) \times 10^9$/L], including lymphocytes, neutrophils, monocytes, eosinophils, and basophils, was observed within the normal physiological range. The observed redistribution of leukocyte subsets into the bloodstream in mice could potentially be influenced by the long-term administration of AMD3100. Nevertheless, the GMNPs@AMD/RAPA group, which involved the combined use of RAPA and AMD3100, did not exhibit this phenomenon. These results indicated that the GMNPs@AMD/RAPA nanosystem did not lead to significant lymphatic depletion. The synergistic utilization of AMD3100 and RAPA demonstrated the effect of maintaining peripheral blood leukocyte homeostasis.

a H&E staining of representative frozen sections of organs from different treatment groups at day 25. Scale bar = 50 μm. **b-m** Complete blood count (CBC) of mice treated with PBS, NPs, RAPA, GMNPs, GMNPs/RAPA, GMNPs@AMD, and GMNPs@AMD/RAPA on day 25. RBC (Red Blood Cells, $\times 10^{12}$/L) (b), Haemoglobin (g/L) (c), MCV (Mean Corpuscular Volume, fL) (d), MCH (Mean Corpuscular Haemoglobin, pg) (e), Reticulocyte Count ($\times 10^9$/L) (f), WBC (White Blood Cells, $\times 10^9$/L) (g), Lymphocyte Count ($\times 10^9$/L) (h), Neutrophil Count ($\times 10^9$/L) (i), Monocyte Count ($\times 10^9$/L) (j), Eosinophil Count ($\times 10^9$/L) (k), Basophil Count ($\times 10^9$/L) (l), Platelet ($\times 10^9$/L) (m). (n = 3).

4. Discussion

This study presents a nanosystem GMNPs@AMD/RAPA that utilizes GBM cell membrane-derived GMNPs as a nanocarrier for targeted and sequential inhibiting the CXCL12/CXCR4 axis and mTOR pathway to reprogram the GBM immune microenvironment and inhibit tumor

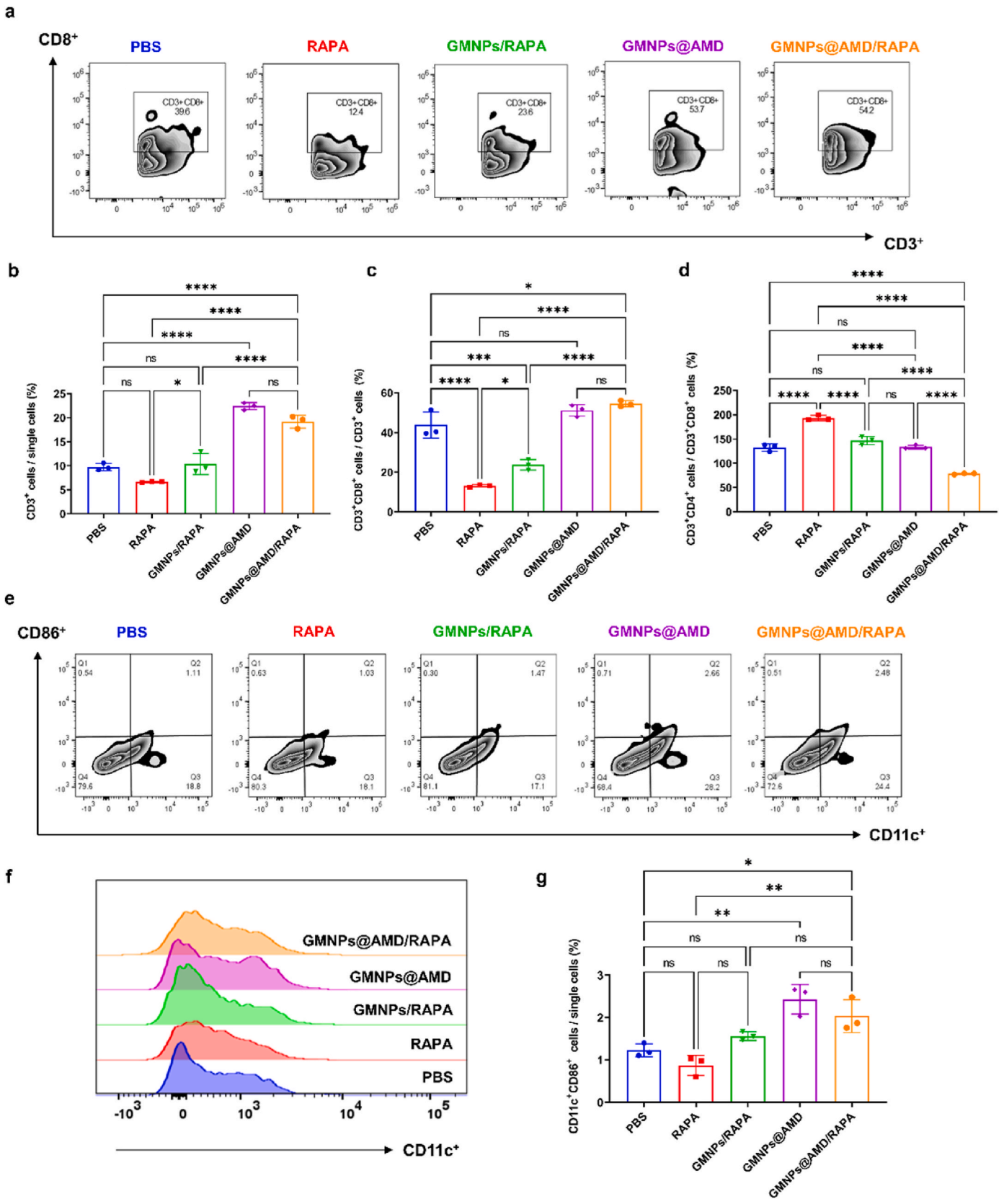

Fig. 6. Immune microenvironment reprogrammed by GMNPs@AMD/RAPA in mice Orthotopic GBM model.

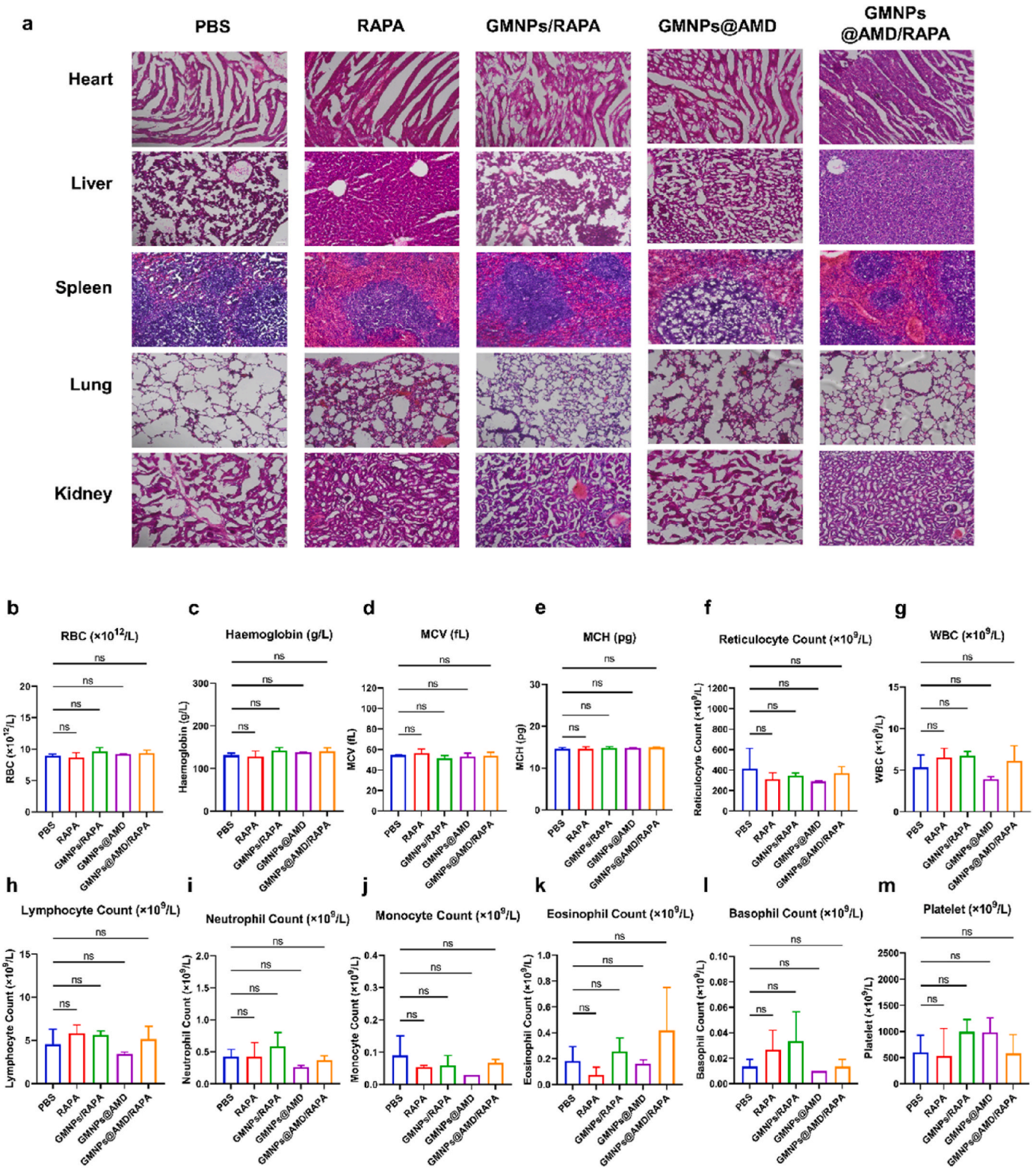

Fig. 7. H&E staining of major organs and hematological safety assessment.

progression (Fig. 1). The inadequate infiltration of CTLs into tumors represents the foremost therapeutic hurdle in the treatment of GBM. Although immunotherapy has emerged as a promising treatment modality in clinical research, it faces challenges such as GBM recurrence resulting from single-agent therapies and limitations due to tumor antigen heterogeneity [36–39]. Therefore, the investigation of sophisticated combinatorial therapies involving chemotherapy and immunotherapy holds tremendous potential in clinical treatment for GBM [5,40–44].

The crosstalk between the CXCL12/CXCR4 axis and PI3K/mTOR pathways plays a crucial role in tumor progression and modulation of the tumor immune microenvironment. In the GMNPs@AMD/RAPA nanosystem, the negatively charged PLGA loaded with RAPA and positively charged AMD3100 through self-assemble undergoes secondary

encapsulation with negatively charged GBM cell membranes, resulting in a stable sequential drug release nanosystem (Fig. 2). Moreover, the biomimetic GBM cell membrane coating enhanced tumor cell targeting and evasion of systematic macrophage clearance (Fig. 4g–i) further enhancing the therapeutic potential of GMNPs@AMD/RAPA in the treatment of GBM. AMD3100, as a CXCR4 antagonist, not only facilitates the infiltration of CTLs into GBM but also inhibits tumor angiogenesis, effectively suppressing the progression of GBM. Furthermore, the dual-layer encapsulation of RAPA within PLGA enables efficient intracellular release in tumor cells, thereby enhancing the antitumor efficacy while minimizing off-target effects and reducing the immunosuppressive effects of RAPA.

Experiments confirm the successful penetration of GMNPs through BBB *in vivo* and *in vitro*, enabling efficient drug delivery (Fig. 3). The co-inhibition of the CXCL12/CXCR4 axis and mTOR pathway leads to synergistic therapeutic effects, resulting in the suppression of tumor cell viability and invasion of GMNPs@AMD/RAPA (Figs. 4 and 5). Additionally, the increased population of activated DCs and $CD8^+$ cytotoxic T cells within the mice GBM microenvironment proves GMNPs@AMD/RAPA is capable of reprogramming the immune microenvironment and modulating the immune-suppressive state (Fig. 6a and c). This rational combination of immunotherapy and chemotherapy in this targeted delivery nanosystem exhibits substantial efficacy and holds considerable potential for clinical applications [45]. Moreover, by simultaneously inhibiting tumor angiogenesis (Fig. 5d) and implementing immunotherapy (Fig. 6), GMNPs@AMD/RAPA improve the efficacy of immunotherapy while mitigating the risk of immune-related adverse reactions (Fig. 7) [46].

5. Conclusion

In summary, we have developed a biomimetic targeted nanosystem that can effectively suppress the progression of GBM and improve the therapeutic outcome of treatment by co-delivery of the CXCR4 antagonists AMD3100 and the mTOR pathway inhibitor RAPA to the TME. Our results demonstrate that by inhibiting the CXCL12/CXCR4 axis, the infiltration of CTLs increased in TME while suppressing the GBM progression. Moreover, in combination with RAPA, the GBM progression was further suppressed, indicating a synergetic effect. In clinical settings, GMNPs@AMD/RAPA can be constructed using patient-derived tissues obtained from biopsies or surgical resections and applied to GBM treatment, promising great potential for accomplishing precision oncology.

CRediT authorship contribution statement

Yulei Mu: Writing – review & editing, Writing – original draft, Methodology, Investigation, Formal analysis, Data curation, Conceptualization. **Zhen Zhang:** Writing – review & editing, Methodology, Investigation, Formal analysis, Data curation, Conceptualization. **Huiqun Zhou:** Validation, Investigation. **Min Jin:** Validation, Investigation. **Liang Ma:** Validation, Investigation. **Bangheng Liu:** Investigation. **Cheng Ma:** Validation, Investigation. **Xu Hu:** Validation, Investigation. **Yi Zhang:** Writing – review & editing, Validation, Resources, Project administration, Funding acquisition, Formal analysis, Conceptualization. **Dong-An Wang:** Writing – review & editing, Supervision, Resources, Project administration, Funding acquisition, Conceptualization.

Declaration of competing interest

The authors declare that they have no known competing financial interests or personal relationships that could have appeared to influence the work reported in this paper.

Data availability

Data will be made available on request.

Acknowledgement

This work was supported by the National Natural Science Foundation of China (NSFC51973180 to Dong-An Wang; and, NSFC62271107 to Yi Zhang); Grants from City University of Hong Kong (SGP7020028, 7006079, 7005949, 9609335 to Dong-An Wang); and Grant from Karolinska Institutet Ming Wai Lau Centre of Reparative Medicine (CityU9231486, 9231412 to Dong-An Wang).

Appendix A. Supplementary data

Supplementary data to this article can be found online at https://doi.org/10.1016/j.mtbio.2024.101222.

References

[1] L.R. Schaff, I.K. Mellinghoff, Glioblastoma and other primary brain malignancies in adults: a review, JAMA 329 (7) (2023) 574–587.
[2] D. Biasci, et al., CXCR4 inhibition in human pancreatic and colorectal cancers induces an integrated immune response, Proc. Natl. Acad. Sci. U. S. A. 117 (46) (2020) 28960–28970.
[3] A. Bikfalvi, et al., Challenges in glioblastoma research: focus on the tumor microenvironment, Trends in cancer 9 (1) (2023) 9–27.
[4] Q.T. Ostrom, et al., Adult glioma incidence and survival by race or ethnicity in the United States from 2000 to 2014, JAMA Oncol. 4 (9) (2018) 1254–1262.
[5] M. Lim, et al., Current state of immunotherapy for glioblastoma, Nat. Rev. Clin. Oncol. 15 (7) (2018) 422–442.
[6] A.C. Tan, et al., Management of glioblastoma: state of the art and future directions, CA A Cancer J. Clin. 70 (4) (2020) 299–312.
[7] Y. Wang, et al., CXCR4-guided liposomes regulating hypoxic and immunosuppressive microenvironment for sorafenib-resistant tumor treatment, Bioact. Mater. 17 (2022) 147–161.
[8] M.J. Smit, et al., The CXCL12/CXCR4/ACKR3 Axis in the tumor microenvironment: signaling, crosstalk, and therapeutic targeting, Annu. Rev. Pharmacol. Toxicol. 61 (2021) 541–563, 61, 2021).
[9] D.-Y. Gao, et al., CXCR4-targeted lipid-coated PLGA nanoparticles deliver sorafenib and overcome acquired drug resistance in liver cancer, Biomaterials 67 (2015) 194–203.
[10] J. Dong, et al., Reversing the PAI-1-induced fibrotic immune exclusion of solid tumor by multivalent CXCR4 antagonistic nano-permeator, Acta Pharm. Sin. B 13 (7) (2023) 3106–3120.
[11] M. Huang, et al., CXCR4 enriched T regulatory cells preferentially home to bone marrow and decrease inflammation, Blood 142 (Supplement 1) (2023), 351-351.
[12] W. Mo, et al., CXCR4/CXCL12 mediate autocrine cell- cycle progression in NF1-associated malignant peripheral nerve sheath tumors, Cell 152 (5) (2013) 1077–1090.
[13] S. Cambier, M. Gouwy, P. Proost, The chemokines CXCL8 and CXCL12: molecular and functional properties, role in disease and efforts towards pharmacological intervention, Cell. Mol. Immunol. 20 (3) (2023) 217–251.
[14] M.M. Steele, et al., T cell egress via lymphatic vessels is tuned by antigen encounter and limits tumor control, Nat. Immunol. 24 (4) (2023) 664–675.
[15] B.A. Teicher, S.P. Fricker, CXCL12 (SDF-1)/CXCR4 pathway in cancer, Clin. Cancer Res. 16 (11) (2010) 2927–2931.
[16] Y. Kang, et al., Plerixafor (Mozobil®) selectively enhances donor hematopoietic cell engraftment, Blood 114 (22) (2009). . 368-368.
[17] J.A. Burger, T.J. Kipps, CXCR4: a key receptor in the crosstalk between tumor cells and their microenvironment, Blood 107 (5) (2006) 1761–1767.
[18] J.S. Song, et al., A highly selective and potent CXCR4 antagonist for hepatocellular carcinoma treatment, Proc. Natl. Acad. Sci. U. S. A. 118 (13) (2021) e2015433118.
[19] M.S. Alghamri, et al., Systemic delivery of an adjuvant CXCR4-CXCL12 signaling inhibitor encapsulated in synthetic protein nanoparticles for glioma immunotherapy, ACS Nano 16 (6) (2022) 8729–8750.
[20] C. Feig, et al., Targeting CXCL12 from FAP-expressing carcinoma-associated fibroblasts synergizes with anti-PD-L1 immunotherapy in pancreatic cancer, Proc. Natl. Acad. Sci. U. S. A. 110 (50) (2013) 20212–20217.
[21] N. Goffart, et al., Adult mouse subventricular zones stimulate glioblastoma stem cells specific invasion through CXCL12/CXCR4 signaling, Neuro Oncol. 17 (1) (2015) 81–94.
[22] M. Guba, et al., Rapamycin inhibits primary and metastatic tumor growth by antiangiogenesis: involvement of vascular endothelial growth factor, Nat. Med. 8 (2) (2002) 128–135.
[23] S. Li, et al., Signaling pathways in brain tumors and therapeutic interventions, Signal Transduct. Targeted Ther. 8 (1) (2023) 8.
[24] V. Panwar, et al., Multifaceted role of mTOR (mammalian target of rapamycin) signaling pathway in human health and disease, Signal Transduct. Targeted Ther. 8 (1) (2023) 375.

[25] J. Jin, Q. Zhao, Emerging role of mTOR in tumor immune contexture: impact on chemokine-related immune cells migration, Theranostics 10 (14) (2020) 6231–6244.
[26] J. Li, D. Oupický, Effect of biodegradability on CXCR4 antagonism, transfection efficacy and antimetastatic activity of polymeric Plerixafor, Biomaterials 35 (21) (2014) 5572–5579.
[27] E. De Clercq, Recent advances on the use of the CXCR4 antagonist plerixafor (AMD3100, Mozobil™) and potential of other CXCR4 antagonists as stem cell mobilizers, Pharmacol. Therapeut. 128 (3) (2010) 509–518.
[28] M. Chehelgerdi, et al., Progressing nanotechnology to improve targeted cancer treatment: overcoming hurdles in its clinical implementation, Mol. Cancer 22 (1) (2023) 169.
[29] R.H. Fang, W. Gao, L. Zhang, Targeting drugs to tumours using cell membrane-coated nanoparticles, Nat. Rev. Clin. Oncol. 20 (1) (2023) 33–48.
[30] T. Yin, et al., Engineered macrophage-membrane-coated nanoparticles with enhanced PD-1 expression induce immunomodulation for a synergistic and targeted antiglioblastoma activity, Nano Lett. 22 (16) (2022) 6606–6614.
[31] R.H. Fang, et al., Cancer cell membrane-coated nanoparticles for anticancer vaccination and drug delivery, Nano Lett. 14 (4) (2014) 2181–2188.
[32] A.V. Kroll, et al., Nanoparticulate delivery of cancer cell membrane elicits multiantigenic antitumor immunity, Adv. Mater. 29 (47) (2017) 1703969.
[33] Z. Yao, et al., Efficiently targeted therapy of glioblastoma xenograft via multifunctional biomimetic nanodrugs, Biomater. Res. 26 (1) (2022) 71.
[34] H. Pan, et al., At the crossroad of nanotechnology and cancer cell membrane coating: expanding horizons with engineered nanoplatforms for advanced cancer therapy harnessing homologous tumor targeting, Coord. Chem. Rev. 506 (2024) 215712.
[35] J.J. Rennick, A.P.R. Johnston, R.G. Parton, Key principles and methods for studying the endocytosis of biological and nanoparticle therapeutics, Nat. Nanotechnol. 16 (3) (2021) 266–276.
[36] P. Zhang, et al., Nanotechnology-enhanced immunotherapy for metastatic cancer, Innovation 2 (4) (2021) 100174.
[37] A. Rotte, J.Y. Jin, V. Lemaire, Mechanistic overview of immune checkpoints to support the rational design of their combinations in cancer immunotherapy, Ann. Oncol. 29 (1) (2018) 71–83.
[38] H.L. Kaufman, F.J. Kohlhapp, A. Zloza, Oncolytic viruses: a new class of immunotherapy drugs, Nat. Rev. Drug Discov. 14 (9) (2015) 642–662.
[39] A.L. Ling, et al., Clinical trial links oncolytic immunoactivation to survival in glioblastoma, Nature 623 (7985) (2023) 157–166.
[40] R. Rahman, et al., Current drug development and trial designs in neuro-oncology: report from the first American society of clinical oncology and society for neuro-oncology clinical trials conference, Lancet Oncol. 24 (4) (2023) e161–e171.
[41] S. Zhou, et al., Reprogramming systemic and local immune function to empower immunotherapy against glioblastoma, Nat. Commun. 14 (1) (2023) 435.
[42] C.G. Drake, Combination immunotherapy approaches, Ann. Oncol. 23 (Suppl 8) (2012) viii41–v46. Suppl 8.
[43] W. Jiang, et al., Considerations for designing preclinical cancer immune nanomedicine studies, Nat. Nanotechnol. 16 (1) (2021) 6–15.
[44] Y. Mu, et al., Applications of nanotechnology in remodeling the tumour microenvironment for glioblastoma treatment, Biomater. Sci 12 (16) (2024) 4045–4064.
[45] F. Meric-Bernstam, et al., Enhancing anti-tumour efficacy with immunotherapy combinations, Lancet 397 (10278) (2021) 1010–1022.
[46] D. Fukumura, et al., Enhancing cancer immunotherapy using antiangiogenics: opportunities and challenges, Nat. Rev. Clin. Oncol. 15 (5) (2018) 325–340.